Article

The seasonal variability of the ocean energy cycle from a quasi-geostrophic double gyre ensemble

Takaya Uchida [1,*,†], Bruno Deremble [1] and Thierry Penduff [1].

[1] Institut des Géosciences de l'Environnement, Centre National de la Recherche Scientifique; Maison Climat-Planete, 460 Rue de la Piscine, 38400 Saint-Martin-d'Hères, France
[2] Department of Earth, Ocean and Atmospheric Science, Florida State University; 1011 Academic Way Tallahassee, FL 32306-4520, USA
* Correspondence: takaya.uchida@univ-grenoble-alpes.fr
† Current address: Institut des Géosciences de l'Environnement, Centre National de la Recherche Scientifique

Abstract: With the advent of submesoscale $O(1\text{ km})$ permitting basin-scale ocean simulations, the seasonality in the mesoscale $O(50\text{ km})$ eddies with kinetic energies peaking in summer has been commonly attributed to submesoscale eddies feeding back onto the mesoscale via an inverse energy cascade under the constraint of stratification and Earth's rotation. In contrast, by running a 101-member, seasonally forced, three-layer quasi-geostrophic (QG) ensemble configured to represent an idealized double-gyre system of the subtropical and subpolar basin, we find that the mesoscale kinetic energy shows a seasonality consistent with the summer peak without resolving the submesoscales; by definition, a QG model only resolves small Rossby number dynamics ($O(Ro) \ll 1$) while as submesoscale dynamics are associated with $O(Ro) \sim 1$. Here, by quantifying the Lorenz cycle of the mean and eddy energy, defined as the ensemble mean and fluctuations about the mean respectively, we propose a different mechanism from the inverse energy cascade by which the stabilization and strengthening of the western-boundary current during summer due to increased stratification leads to a shedding of stronger mesoscale eddies from the separated jet. Conversely, the opposite occurs during the winter; the separated jet destablizes and results in overall lower mean and eddy kinetic energies despite the domain being more susceptible to baroclinic instability from weaker stratification.

Keywords: Ocean circulation; Geostrophic turbulence; Quasi-geostrophic flows

---

1. Introduction

The energy cycle of the atmospheric system, namely the energy exchange between the mean flow and fluctuations about the mean, have long been of interest due to the fluctuating flow being attributed to what is commonly known as the "weather" [1,2]. Similarly, the oceanographic community has had a long-standing interest in eddies, the weather system of the oceans [3,4]. In a seminal paper, Lorenz [2] provided a framework in understanding the eddy-mean flow interaction, a framework often referred to as the Lorenz energy cycle [hereon LEC; 5].

LEC generally decomposes the flow into four energy reservoirs: the mean and eddy available potential energy (APE) and kinetic energy (KE). The concept of APE is perhaps unique to the field of geophysical fluid dynamics where the gravitational force plays a dominant role in the governing equations. Although all geophysical fluids store gravitational potential energy, only a small fraction of it is available to generate fluid motion, hence the prefix "available". The energy exchanges between each reservoir elucidate the balance of physical processes responsible for causing the eddy flow [4]; e.g. exchanges between the mean and eddy KE are associated with barotropic instability while as exchanges between the eddy APE and eddy KE are associated with baroclinic instability. Barotropic instability is generated via horizontal shear in the mean flow while as baroclinic instability occurs when the effect of gravity due to weak vertical stratification becomes on the same order as Earth's rotation [6]. The balance between the two instabilities results in the weather and eddies we commonly observe in the atmosphere and ocean. With the recent increase in computational power and advent of eddy resolving simulations of the ocean, there has

check for updates

Citation: Uchida, T.; Deremble, B.; Penduff, T. The seasonal variability of the ocean energy cycle from a quasi-geostrophic double gyre ensemble. *Preprints* **2021**, *1*, 0.
https://doi.org/

Received:
Accepted:
Published:

Publisher's Note: MDPI stays neutral with regard to jurisdictional claims in published maps and institutional affiliations.

been a growing interest in the interlinkage between the energy exchanges and temporal variability, namely seasonality, in the eddy flow [7,8].

In the context of Physical Oceanography, the eddies can be further separated into meso- and submeso-scale eddies. Mesoscale eddies are roughly on the spatial scales of the Rossby radius ($NH/f_0 \sim O(50 \text{ km})$ where N and H are the vertical stratification and ocean depth respectively, and f_0 is the Coriolis parameter) while as submesoscale eddies are on the scales of $O(1 \text{ km})$ [9]. In terms of Rossby number (Ro $(= U/f_0L)$ where U and L are the characteristic scales of velocity and spatial scale), this translates as mesoscale dynamics being on the order of $O(Ro) \ll 1$ and submesoscale flows being associated with $O(Ro) \sim 1$ [10,11]. In other words, mesoscale dynamics are more constrained by Earth's rotation, leading to the well-known phenomenon of inverse energy cascade where KE is transferred from scales about the Rossby radius to larger scales [12–14]. To what extent the framework of inverse energy cascade is applicable for scales smaller than the Rossby radius remains an open question [10,15,16].

Nevertheless, many studies using meso- and submeso-scale permitting ocean simulations have attributed the seasonality in mesoscale KE to energy being transferred upscale from the submesoscales where the seasonal modulation of the mixed-layer depth leads to a strong signal [11,17–22]. Instabilities within the mixed layer are inherently submesoscale due to the reduced stratification and shallow depth scale, and are most active during late winter/early spring when the mixed-layer is the deepest [23–25]. The summertime peak in mesoscale KE has consequently been explained by the time lag for the submesoscale energy to cascade upscale. While we agree that submesoscale instabilities affect mesoscale variability, here, we examine another mechanism on the other end of the spectrum in modulating the mesoscale seasonality, namely the basin-scale ($O(1000 \text{ km})$) affecting the mesoscale.

In order to quantify the exchanges between the energy reservoirs, we run a seasonally forced, three-layer quasi-geostrophic (QG) ensemble with a double-gyre configuration and examine the LEC. By definition, a QG model only resolves small Rossby number dynamics, i.e. the simulated eddy field only consists of mesoscale variability. The background state in QG can be considered as the basin-scale state. In particular, we define the mean via the ensemble mean and eddies as the fluctuations about the mean. The ensemble mean: i) negates the ergodic assumption where one treats the temporal mean equivalent to an ensemble mean, which is questionable for a temporally varying system; ii) removes the arbitrary temporal and/or spatial scale in defining the mean [26]; iii) is consistent with the Reynold's definition of eddy-mean decomposition [27]; and iv) retains the temporal, namely seasonal, variability of the LEC.

The paper is organized as follows: We describe the model configuration in Section 2 and re-derive the layered QG equations and LEC in Section 3, which will aid our discussion later on. We give our results in Section 4 and conclude in Section 5.

2. Model description

We use the quasi-geostrophic (QG) configuration of the Multiple Scale Ocean Model [MSOM; 28, hereon referred to as MSQG], based on the Basilisk language, to simulate a three-layer double-gyre flow with a rigid lid and flat bottom. No-slip conditions are applied at the lateral boundaries. The parameters used are similar to prior QG studies which examine the dynamics of a double-gyre system [3,29,30] and are summarized in Table 1. The characteristic length scale of the Rossby radius is prescribed as L $(= 50 \text{ km})$ and horizontal resolution is $\sim 15 \text{ km}$ $(= \delta_{\hat{x}} L)$ and so we have roughly three grid points per radius; our simulation can be considered mesoscale resolving [31]. (We note that increasing the resolution does allow for the submesoscales to be permitted in our model due to the QG constraint.) MSQG solves prognostically for the non-dimensionalized QG potential vorticity (PV; q):

$$\frac{D\hat{q}}{D\hat{t}} = \widehat{\mathcal{F}} + \widehat{\mathcal{D}}, \tag{1}$$

Preprints (www.preprints.org) | NOT PEER-REVIEWED | Posted: 12 April 2021 doi:10.20944/preprints202104.0283.v1

where $\mathcal{F}$ and $\mathcal{D}$ are the forcing and dissipative terms, and $\widehat{(\cdot)}$ are non-dimensionalized variables. The background stratification is defined at each layer interface via the Froude number where we enforce the seasonality by varying it in time according to:

$$Fr_i = \frac{U}{\sqrt{g_i' H_i^\dagger}} = Fr_i^m \left[1 + \hat{A}_{Fr_i} \sin\left(2\pi \hat{f}_{Fr_i} \hat{t}\right)\right]^{-1/2}, \tag{2}$$

where $H_i^\dagger = (H_i + H_{i+1})/2$, g' is the reduced gravity, and subscript i is the layer index (Figure 1). We vary Fr_1 in time by keep Fr_2 stationary ($\hat{A}_{Fr_2} = 0$), which is consistent with the seasonal variability of stratification being confined in the upper few hundred meters [32]. The wind stress curl is kept stationary with the formulation:

$$\boldsymbol{\nabla}_\mathrm{h} \times \boldsymbol{\tau}(\hat{y}) = -\frac{\hat{f}_0 \hat{\tau}_0}{\hat{H}_1} \sin\left(\frac{2\pi}{L_0}\hat{y}\right) \sin\left(\frac{\pi}{L_0}\hat{y}\right). \tag{3}$$

Parameter	Notation	Value	Unit
Number of horizontal grids	N	256	-
Number of vertical layers	n_l	3	-
Non-dim. horizontal domain size	$\hat{L}_0$	80	-
Non-dim. horizontal resolution	$\delta_{\hat{x}}$	$N^{-1}\hat{L}_0$	-
Background Rossby number	Ro^m	0.025	-
Non-dim. Coriolis parameter	$\hat{f}_0$	$Ro^{m\,-1}$	-
Bottom Ekman number	Ek^b	0.004	-
Non-dim. surface Ekman pumping	$\hat{\tau}_0$	0.0001	-
Biharmonic Reynolds number	Re_4	1563	-
Non-dim. beta	$\hat{\beta}$	0.5	-
Background Froude number	$Fr_1^m; Fr_2^m$	$0.00409959; 0.01319355$	-
Amplitude of Fr_i	$\hat{A}_{Fr_1}; \hat{A}_{Fr_2}$	$0.1; 0$	-
Non-dim. frequency of Fr_i	$\hat{f}_{Fr_1}; \hat{f}_{Fr_2}$	$62.2^{-1}; 62.2^{-1}$	-
Non-dim. layer thickness	$\widehat{H}_1; \widehat{H}_2; \widehat{H}_3$	$0.06; 0.14; 0.8$	-
Non-dim. reduced gravity	$\widehat{g_i'}$	$Fr_i^{-2}\widehat{H_i^\dagger}$	-
Non-dim. maximum time stepping	$\delta_{\hat{t}}^{\max}$	5×10^{-2}	-
CFL condition	-	0.5	-
Horizontal velocity	U	0.1	[m s^{-1}]
Length scale	L	50	[km]
Total layer thickness	H	5000	[m]

Table 1. Parameters used to configure the three-layer QG simulation and dimensionalized characteristic scales. The bottom Ekman number is the ratio between the bottom Ekman-layer thickness and $\widehat{H}_3$ and bottom friction is $\epsilon = Ek^b/(2Ro^m\widehat{H}_3)$. Beta is dimensionalized as $\beta = \hat{\beta}U/L^2$ and the dimensionalized domain size is 4000 km ($= L_0 L$). The frequency of Fr translates approximately to a 360-day year ($= f_{Fr}^{-1}L/U$). The prognostic time stepping is determined via the CFL condition within values smaller than $\delta_{\hat{t}}^{\max}$.

We spin up the model for 10 years from a spun-up run with stationary stratification ($Fr_i = Fr_i^m$) and then perturb a random single grid in the first-layer stream function field on the order of a floating point error ($O(10^{-31})$) to generate 100 slightly perturbed stream function fields. We use the perturbed fields as the initial conditions to generate 100 ensemble members. The surface wind stress and temporally varying background stratification are kept identical during the spin up and amongst ensemble members after the spin up. We run each ensemble member for another 10 years and for reference, we also have a control (CTRL) run without any perturbations to the initial condition; in total, we have 101 ensemble members and the CTRL run is there to show that the perturbations do

Preprints (www.preprints.org) | NOT PEER-REVIEWED | Posted: 12 April 2021 doi:10.20944/preprints202104.0283.v1

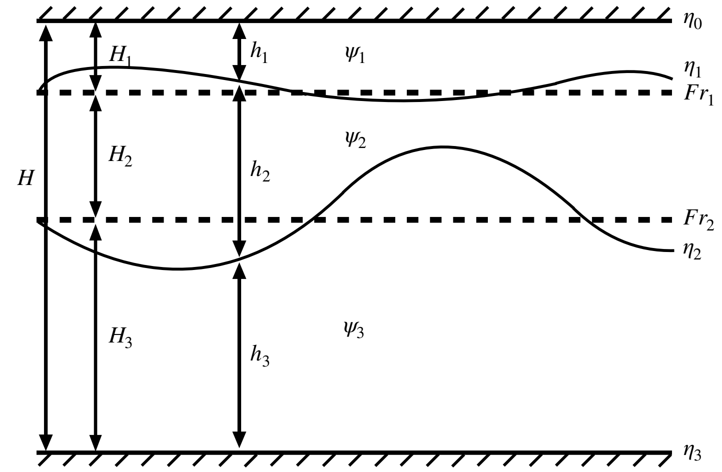

Figure 1. Vertical structure of the three-layer QG model with a rigid lid and flat bottom. The layer interface displacement (η_i) is shown in the thin curvy lines and net layer thickness is $h_i = H_i + \eta_{i-1} - \eta_i$. The stream functions ($\psi_i$) are defined within each layer.

not lead to a bifurcation in the dynamical regime within the 10 years of our simulation [33]. The model outputs were saved as instantaneous snapshots at every characteristic time scale ($\mathcal{T} = L/U = 5 \times 10^5$ seconds).

3. Derivation of the Lorenz energy cycle

Although the layered QG equations have been derived countless times [1,3,6,34], here, we re-derive the energy equations for a rigid-lid and flat-bottom three-layer QG model with a seasonally varying background stratification, which the latter leads to some subtleties. In the remainder of the study, we only discuss dimensionalized variables. We start off with the order Rossby number momentum equations for a given layer i ($\in [1,3]$; Figure 1) neglecting viscous and external forcing terms:

$$\partial_t u_{g;i} + u_{g;i}\partial_x u_{g;i} + v_{g;i}\partial_y u_{g;i} - f_0 v_{a;i} - \beta y v_{g;i} = -\partial_x \phi_{a;i}, \tag{4}$$

$$\partial_t v_{g;i} + u_{g;i}\partial_x v_{g;i} + v_{g;i}\partial_y v_{g;i} + f_0 u_{a;i} + \beta y u_{g;i} = -\partial_y \phi_{a;i}, \tag{5}$$

where the subscripts g and a denote the geostrophic and ageostrophic components respectively ($\boldsymbol{u} = \boldsymbol{u}_g + \boldsymbol{u}_a$) and the β-plane approximation is applied ($f = f_0 + \beta y$). Taking the cross product of the momentum equations leads to the relative vorticity equation:

$$\partial_t \zeta_{g;i} + u_{g;i}\partial_x \zeta_{g;i} + v_{g;i}\partial_y \zeta_{g;i} + \beta v_{g;i} = -f_0(\partial_x u_{a;i} + \partial_y v_{a;i}) \tag{6}$$

$$= f_0 \partial_z w_a, \tag{7}$$

The layer-thickness equation on the other hand is:

$$\partial_t h_i + u_{g;i}\partial_x h_i + v_{g;i}\partial_y h_i = -H_i(\partial_x u_{a;i} + \partial_y v_{a;i}) \tag{8}$$

$$= H_i \partial_z w_a, \tag{9}$$

so equation (6) can be re-written as

$$\frac{D_i}{Dt}\zeta_{g;i} + \beta v_{a;i} = \frac{f_0}{H_i}\frac{D_i}{Dt}h_i, \tag{10}$$

where $\frac{D_i}{Dt} = \partial_t + \boldsymbol{u}_{g;i} \cdot \boldsymbol{\nabla}_\mathrm{h}$ and we get the governing equation for QGPV $q_i = \zeta_{g;i} + \beta y - \frac{f_0}{H_i} h_i$. (The relation between the layered and continuously stratified QG framework is given in Appendix A.) It is perhaps interesting to note that the QGPV remains identical

Preprints (www.preprints.org) | NOT PEER-REVIEWED | Posted: 12 April 2021 doi:10.20944/preprints202104.0283.v1

for a stationary and temporally varying background stratification (viz. $g_1' = \frac{U^2}{H_1^\dagger}Fr_1^{-2}(t)$) although we show below that this is not the case for the energy budget. Now, we can define a stream function as $\psi_i = \phi_{g;i}/f_0$ and relative vorticity becomes $\zeta_{g;i} = \nabla_\mathrm{h}^2\psi_i$. The stream function is related to the layer displacement via $\eta_i = \frac{f_0}{g_i'}(\psi_{i+1} - \psi_i)$. The layer thickness can, therefore, be written using the stream function as:

$$h_i = H_i + \eta_{i-1} - \eta_i \tag{11}$$

$$= H_i + \frac{f_0}{g_{i-1}'}(\psi_i - \psi_{i-1}) - \frac{f_0}{g_i'}(\psi_{i+1} - \psi_i), \tag{12}$$

where $\frac{D_1}{Dt}\eta_0 = \frac{D_3}{Dt}\eta_3 = 0$ due to rigid-lid and flat-bottom boundary conditions. The vertical velocity can be diagnosed via the QG omega equation [Appendix B; 35,36]:

$$N^2\boldsymbol{\nabla}_\mathrm{h}^2 w_a + f_0^2\partial_{zz}w_a = \beta\partial_x b - 2\boldsymbol{\nabla}_\mathrm{h}\cdot\mathbf{Q} - \boldsymbol{\nabla}_\mathrm{h}^2 bN^2\partial_t\frac{1}{N^2}, \tag{13}$$

where $N^2 = g'/H^\dagger$, and $b_i = f_0\frac{\psi_i - \psi_{i+1}}{H_i^\dagger}$ is the buoyancy. The viscous and diffusive terms do not appear as they cancel out due to the thermal-wind relation ($f_0\partial_z\zeta_g = \boldsymbol{\nabla}_\mathrm{h}^2 b$) and their parameters being set identical (viz. $\nu_4 = \kappa_4$ $(= Re_4^{-1}L^3U)$). The $\mathbf{Q}$ tensor is:

$$\mathbf{Q} = Q^1\boldsymbol{i} + Q^2\boldsymbol{j} = (\partial_x\boldsymbol{u}_g^\dagger\cdot\boldsymbol{\nabla}_\mathrm{h}b)\boldsymbol{i} + (\partial_y\boldsymbol{u}_g^\dagger\cdot\boldsymbol{\nabla}_\mathrm{h}b)\boldsymbol{j}, \tag{14}$$

where $\boldsymbol{u}_{g;i}^\dagger = -\partial_y\psi_i^\dagger\boldsymbol{i} + \partial_x\psi_i^\dagger\boldsymbol{j}$ is the geostrophic velocity derived from the inter-facial stream function [$\psi_i^\dagger = \frac{H_i\psi_{i+1} + H_{i+1}\psi_i}{H_i + H_{i+1}}$; 3]. $\boldsymbol{i}$ and $\boldsymbol{j}$ are the horizontal Cartesian unit vectors. The last term on the right-hand side of (13) is due to the temporally varying background stratification (Appendix B). We solved equation (13) iteratively for w_a via a two-dimensional geometric multigrid solver with the boundary conditions of Ekman pumping (w_E):

$$w_{E;0} = -\frac{1}{f_0}\boldsymbol{\nabla}_\mathrm{h}\times\boldsymbol{\tau} = -\frac{UH}{L}\hat{\tau}_0\sin^2\left[\frac{2\pi y}{L_0}\right]\sin\left[\frac{\pi y}{L_0}\right], \tag{15}$$

$$w_{E;3} = \frac{\delta_E}{2}\zeta_{g;3}, \tag{16}$$

where $\delta_E = Ek^b H_3$ is the bottom Ekman-layer thickness.

Now, multiplying equation (7) by $-\psi_i$ and integrating over the depth of each layer gives the kinetic energy (KE) budget:

$$\begin{aligned} H_i\Big[\frac{D_i}{Dt}\frac{|\boldsymbol{\nabla}_\mathrm{h}\psi_i|^2}{2} &- \boldsymbol{\nabla}_\mathrm{h}\cdot(\boldsymbol{u}_{g;i}\psi_i\boldsymbol{\nabla}_\mathrm{h}^2\psi_i) - \frac{\beta}{2}\partial_x\psi_i^2\Big] \\ &= -f_0\int\psi_i\partial_z w_a dz \\ &= f_0\Big[-(w_{a;i-1}\psi_{i-1}^\dagger - w_{a;i}\psi_i^\dagger) + \int w_a\partial_z\psi_i dz\Big] \\ &= f_0\Big[-(w_{a;i-1}\psi_{i-1}^\dagger - w_{a;i}\psi_i^\dagger) + H_i\Big(w_{a;i-1}\frac{\psi_{i-1} - \psi_i}{H_i + H_{i-1}} + w_{a;i}\frac{\psi_i - \psi_{i+1}}{H_{i+1} + H_i}\Big)\Big]. \end{aligned} \tag{17}$$

Dropping the divergence terms as they vanish upon area integration, for each layer we get:

$$\frac{H_1}{2}\partial_t|\boldsymbol{\nabla}_\mathrm{h}\psi_1|^2 = f_0\Big[w_{a;1}\psi_1^\dagger + w_{a;1}H_1\frac{\psi_1 - \psi_2}{H_2 + H_1}\Big], \tag{18}$$

Preprints (www.preprints.org) | NOT PEER-REVIEWED | Posted: 12 April 2021 doi:10.20944/preprints202104.0283.v1

$$\frac{H_2}{2}\partial_t|\boldsymbol{\nabla}_{\mathrm{h}}\psi_2|^2 = f_0\Big[-(w_{a;1}\psi_1^\dagger - w_{a;2}\psi_2^\dagger) + H_2\big(w_{a;1}\frac{\psi_1-\psi_2}{H_2+H_1} + w_{a;2}\frac{\psi_2-\psi_3}{H_3+H_2}\big)\Big], \tag{19}$$

$$\frac{H_3}{2}\partial_t|\boldsymbol{\nabla}_{\mathrm{h}}\psi_3|^2 = f_0\Big[-w_{a;2}\psi_2^\dagger + w_{a;2}H_3\frac{\psi_2-\psi_3}{H_3+H_2}\Big]. \tag{20}$$

On the other hand, using relation (12), the layer-thickness equations can be manipulated as $\frac{H_2}{H_1+H_2}(9)|_{i=1} - \frac{H_1}{H_1+H_2}(9)|_{i=2}$:

$$\begin{aligned}\frac{D_1^\dagger}{Dt}\Big[\frac{f_0}{g_1'}(\psi_1-\psi_2)\Big] &= -w_{a;1} + \frac{H_1}{H_1+H_2}\Big[w_{a;2} - \frac{D_2}{Dt}\frac{f_0}{g_2'}(\psi_3-\psi_2)\Big]\\ &= -w_{a;1} - \frac{f_0H_1}{g_2'(H_1+H_2)}(\boldsymbol{u}_2-\boldsymbol{u}_3)\cdot\boldsymbol{\nabla}_{\mathrm{h}}(\psi_2-\psi_3)\\ &= -w_{a;1},\end{aligned} \tag{21}$$

where the second term on the right-hand side above (21) vanishes due to thermal wind. Similarly, $\frac{H_3}{H_2+H_3}(9)|_{i=2} - \frac{H_2}{H_2+H_3}(9)|_{i=3}$:

$$\begin{aligned}\frac{D_2^\dagger}{Dt}\Big[\frac{f_0}{g_2'}(\psi_2-\psi_3)\Big] &= -w_{a;2} + \frac{H_3}{H_2+H_3}\Big[w_{a;1} - \frac{D_2}{Dt}\frac{f_0}{g_1'}(\psi_2-\psi_1)\Big]\\ &= -w_{a;2},\end{aligned} \tag{22}$$

where $\frac{D_i^\dagger}{Dt} = \partial_t + \boldsymbol{u}_{g;i}^\dagger\cdot\boldsymbol{\nabla}_{\mathrm{h}}$. The available potential energy (APE) equations can, therefore, be derived by multiplying equation (21) with $f_0(\psi_1-\psi_2)$ and again dropping the divergence terms:

$$\partial_t\Big[\frac{f_0^2}{2g_1'}(\psi_1-\psi_2)^2\Big] = -f_0(\psi_1-\psi_2)w_{a;1} - \frac{f_0^2(\psi_1-\psi_2)^2}{2}\partial_t g_1'^{-1}, \tag{23}$$

and equation (22) with $f_0(\psi_2-\psi_3)$:

$$\partial_t\Big[\frac{f_0^2}{2g_2'}(\psi_2-\psi_3)^2\Big] = -f_0(\psi_2-\psi_3)w_{a;2}. \tag{24}$$

We see from equation (23) that there is an additional source of APE due to the temporally varying background potential energy (BPE; $B^\#$), which then feeds back onto the KE via equations (18) and (19) through baroclinic instability. BPE takes the same form as APE except that only g' is inside the derivative.

Now, the mean KE (MKE; $K^\#$), eddy KE (EKE; $\mathcal{K}$), mean APE (MAPE; $P^\#$) and eddy APE (EAPE; $\mathcal{P}$) can be defined as:

$$K_i^\# = \frac{H_i}{2}|\boldsymbol{\nabla}_{\mathrm{h}}\overline{\psi_i}|^2,\ \mathcal{K}_i = \frac{H_i}{2}\overline{|\boldsymbol{\nabla}_{\mathrm{h}}\psi_i'|^2}, \tag{25}$$

$$P_i^\# = \frac{f_0^2}{2g_i'}(\overline{\psi_i} - \overline{\psi_{i+1}})^2,\ \mathcal{P}_i = \frac{f_0^2}{2g_i'}\overline{(\psi_i' - \psi_{i+1}')^2}, \tag{26}$$

where $\overline{(\cdot)}$ is the ensemble mean and the eddy is defined as fluctuations about the ensemble mean, viz. $(\cdot)' = (\cdot) - \overline{(\cdot)}$. We note that the ensemble mean of the fluctuations vanish ($\overline{(\cdot)'} = 0$). The strength of defining the mean as such is that in addition to the ensemble-mean operator commuting with the derivatives with respect to (t, z, y, x) [27], it provides a unique decomposition between the mean and eddy. In other words, the mean does not depend on an arbitrary temporal or spatial scale, which is beneficial in our case as the separated jet is on QG scaling in the cross-jet direction while as on planetary-geostrophic scaling in the along-jet direction [37,38]. The ensemble mean can be interpreted as the QG response to external forcing while as the eddies as a result of intrinsic variability arising at QG scales [39–41]. The ensemble mean of total KE and APE each satisfy $\overline{K_i} = \frac{H_i}{2}\overline{|\nabla_\mathrm{h}\psi_i|^2} = K_i^\# + \mathcal{K}_i$, $\overline{P_i} = \frac{f_0^2}{2g'_i}\overline{(\psi_i - \psi_{i+1})^2} = P_i^\# + \mathcal{P}_i$. Hence, the exchanges ($\Pi$) of KE and APE within and between layers are:

$$\Pi_{K_1^\#\to\mathcal{K}_1} = -H_1\langle\overline{\psi_1}\boldsymbol{\nabla}_\mathrm{h}\cdot\overline{\boldsymbol{u}'_{g;1}\boldsymbol{\nabla}^2_\mathrm{h}\psi'_1}\rangle, \tag{27}$$

$$\Pi_{K_1^\#\to K_2^\#} = -f_0\langle\overline{w}_{a;1}\overline{\psi_1^\dagger}\rangle,\;\; \Pi_{\mathcal{K}_1\to\mathcal{K}_2} = -f_0\langle\overline{w'_{a;1}\psi_1^{\dagger\prime}}\rangle, \tag{28}$$

$$\Pi_{P_1^\#\to K_1^\#} = \frac{f_0H_1}{H_2+H_1}\langle\overline{w}_{a;1}(\overline{\psi_1}-\overline{\psi_2})\rangle,\;\; \Pi_{\mathcal{P}_1\to\mathcal{K}_1} = \frac{f_0H_1}{H_2+H_1}\langle\overline{w'_{a;1}(\psi'_1-\psi'_2)}\rangle, \tag{29}$$

$$\Pi_{P_1^\#\to\mathcal{P}_1} = -\frac{f_0^2}{g'_1}\langle(\overline{\psi_1}-\overline{\psi_2})\boldsymbol{\nabla}_\mathrm{h}\cdot\overline{\boldsymbol{u}^{\dagger}_{g;1}{}'(\psi'_1-\psi'_2)}\rangle, \tag{30}$$

$$\Pi_{B_1^\#\to P_1^\#} = -\frac{f_0^2}{2}\langle(\overline{\psi_1}-\overline{\psi_2})^2\partial_t\overline{g_1'^{-1}}\rangle,\;\; \Pi_{B_1^\#\to\mathcal{P}_1} = -\frac{f_0^2}{2}\langle\overline{(\psi'_1-\psi'_2)^2\partial_t g_1'^{-1}}\rangle, \tag{31}$$

$$\Pi_{K_2^\#\to\mathcal{K}_2} = -H_2\langle\overline{\psi_2}\boldsymbol{\nabla}_\mathrm{h}\cdot\overline{\boldsymbol{u}'_{g;2}\boldsymbol{\nabla}^2_\mathrm{h}\psi'_2}\rangle, \tag{32}$$

$$\Pi_{K_2^\#\to K_3^\#} = -f_0\langle\overline{w}_{a;2}\overline{\psi_2^\dagger}\rangle,\;\; \Pi_{\mathcal{K}_2\to\mathcal{K}_3} = -f_0\langle\overline{w'_{a;2}\psi_2^{\dagger\prime}}\rangle, \tag{33}$$

$$\Pi_{P_1^\#\to K_2^\#} = \frac{f_0H_2}{H_2+H_1}\langle\overline{w}_{a;1}(\overline{\psi_1}-\overline{\psi_2})\rangle,\;\; \Pi_{\mathcal{P}_1\to\mathcal{K}_2} = \frac{f_0H_2}{H_2+H_1}\langle\overline{w'_{a;1}(\psi'_1-\psi'_2)}\rangle, \tag{34}$$

$$\Pi_{P_2^\#\to K_2^\#} = \frac{f_0H_2}{H_3+H_2}\langle\overline{w}_{a;2}(\overline{\psi_2}-\overline{\psi_3})\rangle,\;\; \Pi_{\mathcal{P}_2\to\mathcal{K}_2} = \frac{f_0H_2}{H_3+H_2}\langle\overline{w'_{a;2}(\psi'_2-\psi'_3)}\rangle, \tag{35}$$

$$\Pi_{P_2^\#\to\mathcal{P}_2} = -\frac{f_0^2}{g'_2}\langle(\overline{\psi_3}-\overline{\psi_2})\boldsymbol{\nabla}_\mathrm{h}\cdot\overline{\boldsymbol{u}^{\dagger}_{g;3}{}'(\psi'_3-\psi'_2)}\rangle, \tag{36}$$

$$\Pi_{K_3^\#\to\mathcal{K}_3} = -H_3\langle\overline{\psi_3}\boldsymbol{\nabla}_\mathrm{h}\cdot\overline{\boldsymbol{u}'_{g;3}\boldsymbol{\nabla}^2_\mathrm{h}\psi'_3}\rangle, \tag{37}$$

$$\Pi_{P_2^\#\to K_3^\#} = \frac{f_0H_3}{H_2+H_3}\langle\overline{w}_{a;2}(\overline{\psi_2}-\overline{\psi_3})\rangle,\;\; \Pi_{\mathcal{P}_2\to\mathcal{K}_3} = \frac{f_0H_3}{H_3+H_2}\langle\overline{w'_{a;2}(\psi'_2-\psi'_3)}\rangle, \tag{38}$$

where $\langle\cdot\rangle = \iint(\cdot)dxdy$ is the area integration. Further details regarding the sign convention and forcing/dissipation terms are given in Appendix C and D. Summing up each layer gives the volume integrated energy exchanges:

$$\Pi_{P^\#\to K^\#} = \sum_{i=1}^{2} f_0\langle\overline{w}_{a;i}(\overline{\psi_i}-\overline{\psi_{i+1}})\rangle, \tag{39}$$

$$\Pi_{\mathcal{P}\to\mathcal{K}} = \sum_{i=1}^{2} f_0\langle\overline{w'_{a;i}(\psi'_i-\psi'_{i+1})}\rangle, \tag{40}$$

$$\Pi_{P^\#\to\mathcal{P}} = \frac{f_0^2}{g'_1}\langle(\overline{\psi_1}-\overline{\psi_2})\boldsymbol{\nabla}_\mathrm{h}\cdot\overline{\boldsymbol{u}'_{g;1}(\psi'_1-\psi'_2)}\rangle + \frac{f_0^2}{g'_2}\langle(\overline{\psi_2}-\overline{\psi_3})\boldsymbol{\nabla}_\mathrm{h}\cdot\overline{\boldsymbol{u}'_{g;3}(\psi'_2-\psi'_3)}\rangle, \tag{41}$$

$$\Pi_{K^\#\to\mathcal{K}} = -\sum_{i=1}^{3} H_i\langle\overline{\psi_i}\boldsymbol{\nabla}_\mathrm{h}\cdot\overline{\boldsymbol{u}'_{g;i}\boldsymbol{\nabla}^2_\mathrm{h}\psi'_i}\rangle, \tag{42}$$

$$\Pi_{B^\#\to P^\#} = -\frac{f_0^2}{2}\langle(\overline{\psi_1}-\overline{\psi_2})^2\partial_t\overline{g_1'^{-1}}\rangle, \tag{43}$$

$$\Pi_{B^\#\to\mathcal{P}} = -\frac{f_0^2}{2}\langle\overline{(\psi'_1-\psi'_2)^2\partial_t g_1'^{-1}}\rangle. \tag{44}$$

Preprints (www.preprints.org) | NOT PEER-REVIEWED | Posted: 12 April 2021 doi:10.20944/preprints202104.0283.v1

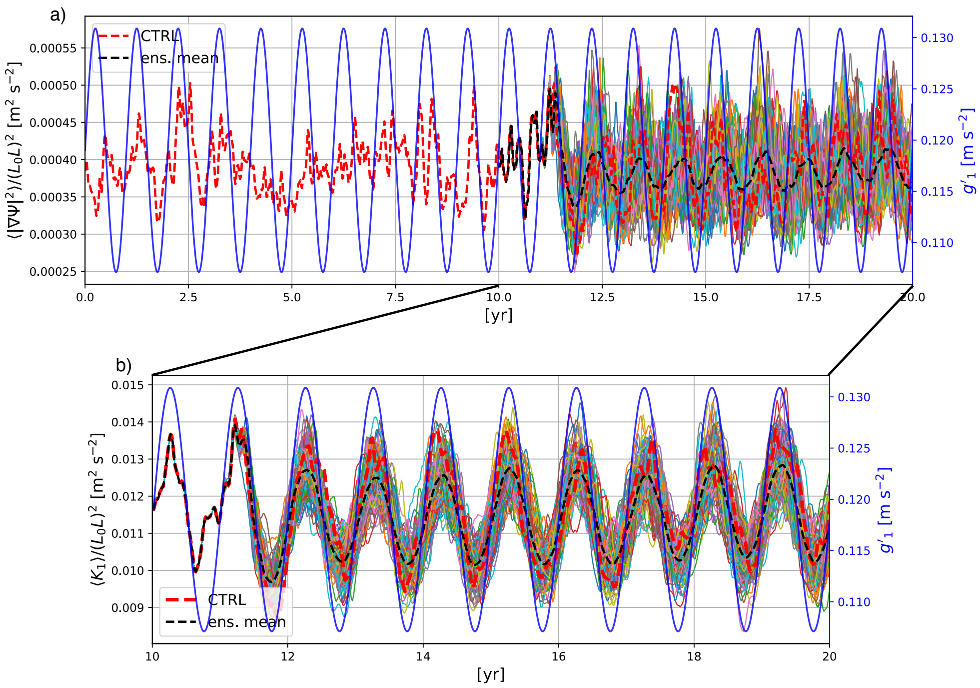

Figure 2. Time series of the horizontally averaged barotropic **a** and first-layer TKE **b**. Each ensemble member is shown in the thin colored lines. The reduced gravity is shown in blue plotted against the right y axes. The CTRL run is shown in red-dashed and ensemble mean in black dashed lines respectively.

4. Results

We start by showing the total kinetic energy (TKE) during the spin-up phase and for the 10 years of output we have (viz. 20 years in total; Figure 2). The ensemble spread starts to grow after a year of integration and plateaus roughly for the latter eight years. The area-integrated TKE in the first layer ($\langle K_1 \rangle$), most relevant for studies interested in surface seasonal dynamics, is in sync with the background stratification (g'_1), viz. higher $\langle K_1 \rangle$ during summer when stratification is stronger and visa versa (Figure 2b). For the lower layers, there is a temporal lag evident by the barotropic TKE ($\langle|\boldsymbol{\nabla}_\mathrm{h}\Psi|^2\rangle$ where $\Psi = H^{-1}\sum_i H_i\psi_i$ is the barotropic stream function; Figure 2a). Although it is difficult to detect a clear seasonal signal for the barotropic TKE from each individual ensemble member, their ensemble mean shows a robust seasonality. For the remainder of the study, we use the last four years of output in order to maximize the signal of intrinsic variability amongst members.

In Figure 3, we show the mean and eddy KE respectively in the first layer ($K_1^{\#}, \mathcal{K}_1$) during summer for the last year of output and their difference from wintertime. The fields were taken at the time step when the reduced gravity was at its maximum and minimum. We see the characteristic feature of a robust separated western boundary current in a double-gyre system with very little meandering while as the EKE is more meridionally spread out. Consistent with Figure 2, summertime has a stronger mean jet and EKE than winter (Figure 3c,d). We also show snapshots of eddy PV ($q'_{g;1}$) from the CTRL run from which we see coherent features of mesoscale eddies (Figure 3e,f).

4.1. The domain integrated Lorenz energy cycle

We now move on to quantifying the LEC in order to examine the processes responsible for generating higher KE during summertime. As we define the mean as the ensemble mean (as opposed to a temporal mean which has commonly been applied), we are able to examine the temporal variability of LEC. We compute the terms in equations (39)-(44) for the last four years of output and show them in Figure 4. The time series of the mean energy

Preprints (www.preprints.org) | NOT PEER-REVIEWED | Posted: 12 April 2021 doi:10.20944/preprints202104.0283.v1

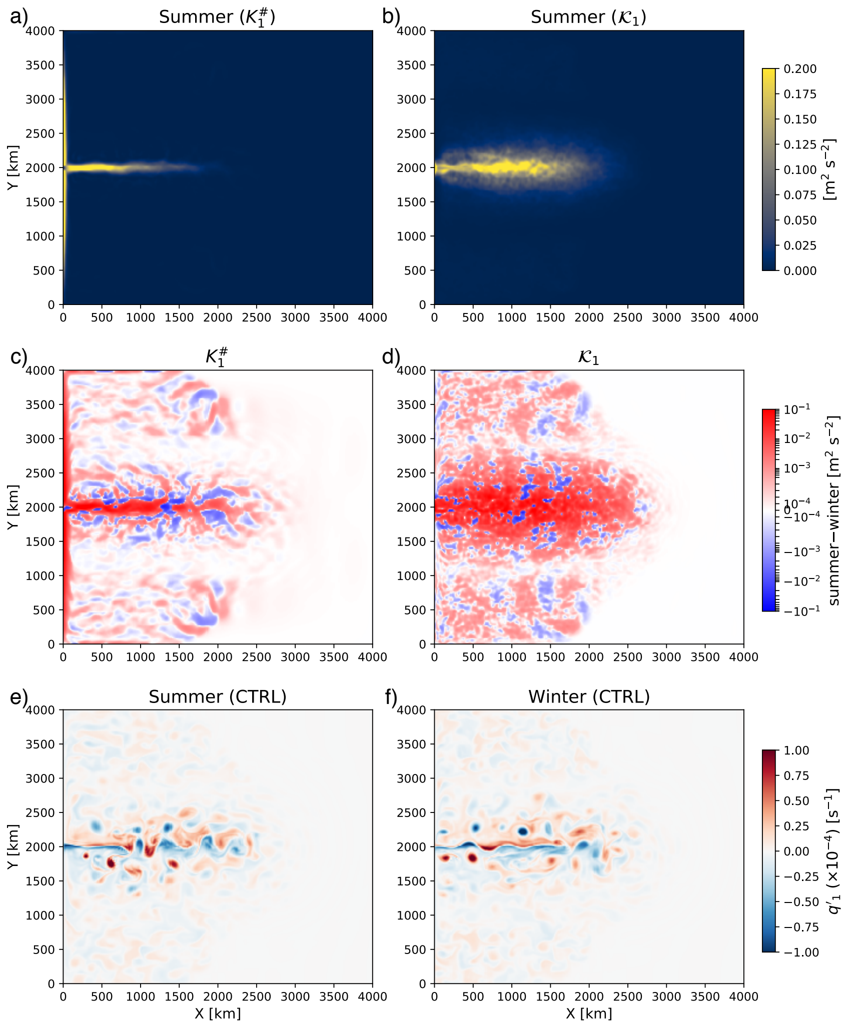

Figure 3. The summertime mean and eddy KE and their difference with winter **a-d**. Note the differences are plotted on a logarithmic scale. **e**,**f** Snapshot of eddy PV for summer and winter during the last year of output. The fields show the first layer and the eddy PV is taken from the CTRL run.

Preprints (www.preprints.org) | NOT PEER-REVIEWED | Posted: 12 April 2021 doi:10.20944/preprints202104.0283.v1

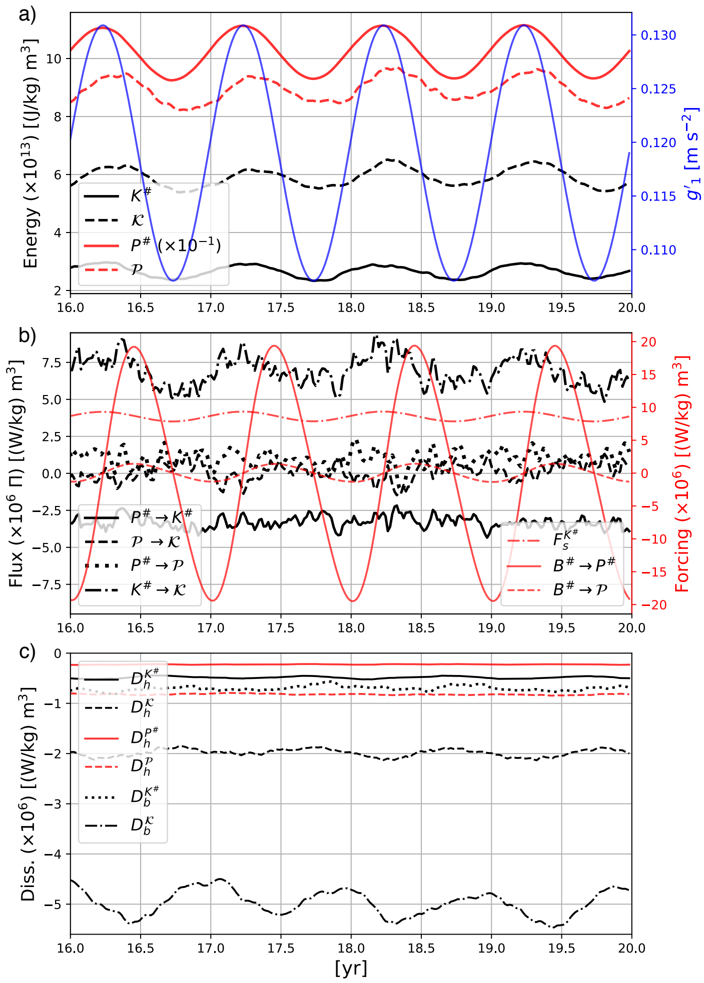

Figure 4. Time series of each term in the domain-integrated LEC. **a** The mean and eddy KE (black) and APE (red) reservoirs in the units of $\times 10^{13}$ [(J/kg) m^3] and stratification of the first layer interface (blue; g_1'). MAPE is multiplied by 0.1 to have it fit on the same y axis. **b** The energy fluxes between each energy reservoir and forcing terms due to surface wind stress ($F_s^{K^\#}$) and temporally varying BPE. **c** Dissipation terms due to horizontal viscosity (D_h) and bottom friction (D_b). The fluxes are in the units of $\times 10^6$ [(W/kg) m^3].

reservoirs are in sync with the background stratification; the mean energy is highest during summer and visa versa ($P^\#, K^\#$; Figure 4a). The eddy reservoirs, on the other hand, lag the stratification by ~ 1 months but their peaks precede winter when the domain is most susceptible to baroclinic instability ($\mathcal{P}, \mathcal{K}$; Figure 4a). MAPE has the largest magnitude amongst the reservoirs by an order of magnitude and for KE, the eddies are more energetic than the mean. The energy flux from MAPE to MKE is always negative ($\Pi_{P^\# \to K^\#} < 0$) due to Ekman pumping. Although the energy input due to wind stress ($F_s^{K^\#}$) is in sync with MKE with energetic currents resulting in stronger surface stress, $\Pi_{P^\# \to K^\#}$ does not show a seasonal fluctuation (Figures 4b and 5a). This is likely due to the bottom drag counter balancing the wind energy input (D_b in Figure 4c).

To provide a climatological view of the energy fluxes (Π), we take the yearly average of the last four years and show the LEC diagram for a climatological summer and winter (Figure 5). Each season per year is defined as three time steps; summer is when the reduced gravity takes its maxima and one time step each before and after the peak, and three time steps about the minima in reduced gravity for winter. The seasonal climatology is then taken as the average of the four years. Again, we see that all reservoirs are more energetic during the summer. Focusing on MKE, except for the surface wind stress, the

Preprints (www.preprints.org) | NOT PEER-REVIEWED | Posted: 12 April 2021 doi:10.20944/preprints202104.0283.v1

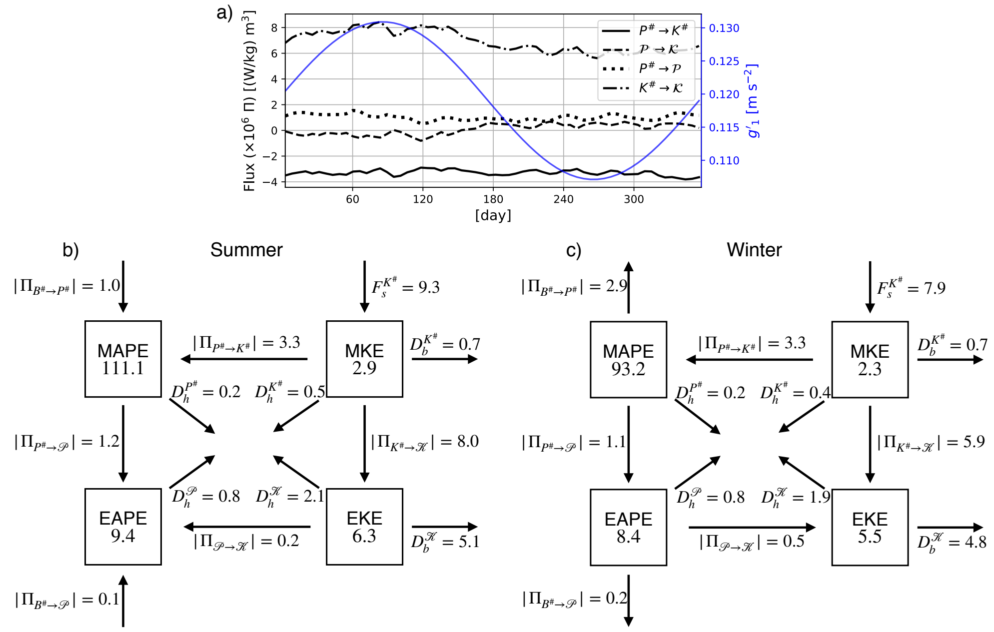

Figure 5. Time series of the seasonal climatology of energy fluxes between the energy reservoirs **a**. **b**,**c** The LEC diagram for the climatological summer and winter averaged over the last four years of output. The energies are in the units of $\times 10^{13}$ [(J/kg) m^3] and fluxes are in $\times 10^6$ [(W/kg) m^3]. The energy exchanges do not exactly cancel out due to each reservoir having temporal variability.

reservoir only has loss terms year round and yet stores more energy during the summer. We attribute this to the separated jet stabilizing due to increased stratification, which results in the jet shedding stronger eddies. Indeed the energy flux from MKE to EKE ($\Pi_{\mathcal{K}^\# \to \mathcal{K}}$) is highest during the summer (Figures 4b and 5a). It is perhaps interesting to note that the sign of fluxes between EAPE and EKE reverses depending on the season with barotropic instability dominating over baroclinic instability during summer; the energy pathway becomes MKE→EKE→EAPE ($\Pi_{\mathcal{P}\to\mathcal{K}} < 0$) during summer whereas baroclinic instability would predict EAPE→EKE ($\Pi_{\mathcal{P}\to\mathcal{K}} > 0$).

4.2. Time lag for vertical barotropization

In this section, we investigate the mechanism for the lag in KE in the lower layers (K_2, K_3) from KE in the first layer (K_1) and stratification (g_1') as evident from Figure 2. Although the oceanographic community has had an emphasis on the surface horizontal inverse energy cascade, rightly so with satellite observations of the global sea surface [13,42], we hypothesize the temporal lag in our model is caused by the vertical inverse energy cascade, i.e. barotropization of the flow [6]. We can quantify this by examining the KE transfers to lower layers (equations (28) and (33)). From Figure 4a, the mean reservoirs do not show a temporal lag so we will focus only on the EKE reservoirs. In Figure 6, we show the timeseries of $\Pi_{\mathcal{K}_1\to\mathcal{K}_2}$ and $\Pi_{\mathcal{K}_2\to\mathcal{K}_3}$; taking the lag correlation, $\Pi_{\mathcal{K}_1\to\mathcal{K}_2}$ lags g_1' by $\sim$ 12 days and $\Pi_{\mathcal{K}_2\to\mathcal{K}_3}$ lags g_1' by $\sim$ 23 days. The temporal lags roughly agree with the $\sim$ 1 month lag we see for EKE and EAPE in Figure 4a.

5. Discussion and conclusions

By running a seasonally forced 101-member ensemble of a three-layer quasi-geostrophic (QG) model in an idealized double-gyre configuration, we have shown that the kinetic energy (KE) peaks during summer when the (basin-scale) stratification is strongest during the year (Figure 2). Such seasonality in mesoscale eddy KE (EKE) has been observed in other studies using realistic simulations of the ocean [11,18–22]. Due to air-sea interaction, the seasonal modulation of the mixed-layer depth leads to a strong seasonal signal in sub-mesoscale instabilities. The submesoscale EKE takes its maximum during late winter/early

Preprints (www.preprints.org) | NOT PEER-REVIEWED | Posted: 12 April 2021 doi:10.20944/preprints202104.0283.v1

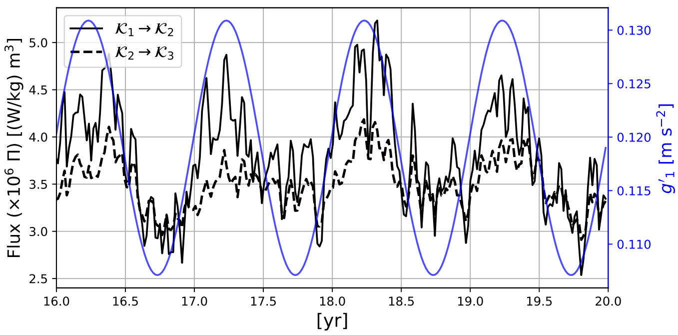

Figure 6. Timeseries of the EKE exchanges between layers ($\Pi_{\mathcal{K}_1 \rightarrow \mathcal{K}_2}$ and $\Pi_{\mathcal{K}_2 \rightarrow \mathcal{K}_3}$) plotted along with the reduced gravity (g'_1).

spring and previous studies have commonly explained the summer peak in the mesoscale range as the time lag for the submesoscale EKE to cascade upscale. The mechanism of inverse energy cascade fails, however, to explain the mesoscale seasonality in our model as a QG model by definition cannot resolve any submesoscale instabilities.

Using the framework of the Lorenz energy cycle [LEC; 2], we have quantified the reservoirs of mean and eddy available potential energy (APE) and KE, and energy fluxes amongst them. We note that our ensemble framework has allowed us to examine the seasonal variability of LEC. Our results show that all four reservoirs store more energy during the summer than winter (Figure 4a). For the mean KE (MKE), we attribute the summertime maximum to increased stratification leading to a more baroclinically stable and stronger jet. Conceptually, this can be understood based on a mass-flux balance. Since the wind stress is kept stationary, the Sverdrup transport ($\beta^{-1}\boldsymbol{\nabla}_{\mathrm{h}} \times \boldsymbol{\tau}$) remains constant throughout the simulation. Based on mass balance, the accumulating transport towards the north/south boundaries must be fluxed out via the western boundary current. Figure 3c shows an intensification of MKE during summer along the western boundary resulting from less energy lost to the eddies within the gyre interior. Hence, a more stable jet results in a stronger mean flow.

Shifting our focus to EKE, based on baroclinic instability, one might expect the opposite to be true, namely, wintertime having more EKE than summertime due to weaker stratification. The LEC shows that during summer, energy fluxes from MKE to EKE associated with barotropic instability over compensate for the fluxes from eddy APE (EAPE) to EKE, a pathway associated with baroclinic instability. Since MKE is higher during summer, the larger flux of energy from MKE to EKE results in EKE peaking in summer (Figures 4b and 5). Although our simulation is highly idealized, we argue that barotropic processes dominating in the separated jet region is consistent with a recent study on energetics using a realistic simulation of the North Atlantic Ocean [38].

To our knowledge, Qiu et al. [17] is the only study using a realistic ocean simulation showing how the seasonality in background state can modulate the mesoscale variability. Their results differ from ours, however, in that they attribute the mesoscale seasonality to the classical Phillips-like baroclinic instability arising from the interior background stratification and vertical shear in horizontal velocity [1]. In addition to the submesoscale variability modulating mesoscale seasonality, our results suggest that in reality it is possible that the basin-scale variability does so as well. We note that since our QG model does not permit submesoscales, the baroclinic energy flux from EAPE to EKE is likely underestimated compared to the real ocean. It would be interesting to revisit the LEC for realistic ocean ensembles [41,43] to see whether we would see a stabilization of the separated Gulf Stream during summer and consequently larger energy fluxes from MKE to EKE.

Author Contributions: Conceptualization, T.U.; methodology, T.U. & B.D.; software, B.D.; validation, T.U., B.D.; formal analysis, T.U.; investigation, T.U. & B.D.; computational resources, T.P.; data

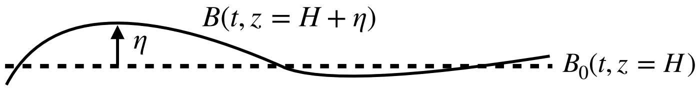

Figure A1. Schematic of a relation between buoyancy (B) and layer interface displacement (η). The background buoyancy is B_0 defined at $z = H$.

curation, T.U.; writing, T.U.; visualization, T.U.; project administration, T.P.; funding acquisition, T.P. All authors have read and agreed to the published version of the manuscript.

Funding: This research was funded by the French 'Make Our Planet Great Again' (MOPGA) initiative managed by the Agence Nationale de la Recherche under the Programme d'Investissement d'Avenir, with the reference ANR-18-MPGA-0002. We acknowledge high-performance computing resources for analyzing our model outputs on Occigen maintained by CINES with the reference A0090112020.

Institutional Review Board Statement: Not applicable.

Informed Consent Statement: Not applicable.

Data Availability Statement: The last time step of the ensemble stream function and example analysis code in Python is available on Github (`doi:10.5281/zenodo.4667532`). For more output files, please contact the corresponding author.

Acknowledgments: We thank William K. Dewar for his always insightful and fruitful discussion. The authors would like to acknowledge the developers of the Basilisk language (http://basilisk.fr/) upon which MSOM is based on, and the developers of the `xarray` Python package [44], which we used to post process the model outputs.

Conflicts of Interest: The authors declare no conflict of interest. The funders had no role in the design of the study; in the collection, analyses, or interpretation of data; in the writing of the manuscript, or in the decision to publish the results.

Appendix A. Relation between the layered and continuously stratified QG framework

Suppose at any given time, we have total buoyancy (B) defined on a layer interface (Figure A1). Based on Taylor expansion, the layer interface displacement can be expanded as [6]:

$$\eta = \frac{\partial z}{\partial B}\Big|_{z=H} [B_0(t, z = H) - B(t, z = H + \eta)] \tag{A1}$$

$$= -\frac{\partial z}{\partial B}\Big|_{z=H} b, \tag{A2}$$

where $b = B - B_0$ is the QG fluctuations about the background buoyancy (B_0). Hence, we get:

$$\frac{b}{N^2} = -\eta, \tag{A3}$$

and taking the material derivative gives the buoyancy equation:

$$\frac{D}{Dt}\frac{b}{N^2} = -w. \tag{A4}$$

Equation (A3) gives the physical intuition that the material derivative of b/N^2 leads to vortex stretching.

Appendix B. The omega equation with a temporally varying background stratification

We derive the QG omega equation using the continuously stratified framework. Taking the vertical derivative of the momentum equations (4) and (5) multiplied by f_0 gives:

$$\frac{D}{Dt}(f_0 \partial_z u_g) + \partial_y \boldsymbol{u}_g \cdot \boldsymbol{\nabla}_{\mathrm{h}} b - f_0^2 \partial_z v_a - \beta y f_0 \partial_z v_g = 0, \tag{A5}$$

$$\frac{D}{Dt}(f_0\partial_z v_g) - \partial_x \boldsymbol{u}_g \cdot \boldsymbol{\nabla}_{\mathrm{h}} b + f_0^2 \partial_z u_a + \beta y f_0 \partial_z u_g = 0, \tag{A6}$$

and the horizontal gradients of the buoyancy equation (A4) yields:

$$\frac{1}{N^2}\frac{D}{Dt}\partial_x b + \partial_x b \partial_t \frac{1}{N^2} + \frac{\partial_x \boldsymbol{u}_g}{N^2} \cdot \boldsymbol{\nabla}_{\mathrm{h}} b + \partial_x w_a = 0, \tag{A7}$$

$$\frac{1}{N^2}\frac{D}{Dt}\partial_y b + \partial_y b \partial_t \frac{1}{N^2} + \frac{\partial_y \boldsymbol{u}_g}{N^2} \cdot \boldsymbol{\nabla}_{\mathrm{h}} b + \partial_y w_a = 0. \tag{A8}$$

Summing equation (A5) with (A8), and $-$(A6) with (A7), and using the thermal wind relation, we get:

$$2\partial_y \boldsymbol{u}_g \cdot \boldsymbol{\nabla}_{\mathrm{h}} b + N^2 \partial_y w_a - \beta y \partial_x b - f_0^2 \partial_z v_a + \partial_y b N^2 \partial_t \frac{1}{N^2} = 0. \tag{A9}$$

$$2\partial_x \boldsymbol{u}_g \cdot \boldsymbol{\nabla}_{\mathrm{h}} b + N^2 \partial_x w_a + \beta y \partial_y b - f_0^2 \partial_z u_a + \partial_x b N^2 \partial_t \frac{1}{N^2} = 0, \tag{A10}$$

Taking ∂_y(A9)+∂_x(A10) gives the omega equation for a temporally varying background stratification:

$$N^2 \boldsymbol{\nabla}_{\mathrm{h}}^2 w_a + f_0^2 \partial_{zz} w_a = \beta \partial_x b - 2\boldsymbol{\nabla}_{\mathrm{h}} \cdot \mathbf{Q} - \boldsymbol{\nabla}_{\mathrm{h}}^2 b N^2 \partial_t \frac{1}{N^2}. \tag{A11}$$

Although the last on the right-hand side involves a time derivative, there is no time dependency in our case as we know the analytical form of the background stratification (equation (2)). Its contribution to the omega equation turned out to be negligible (not shown).

Appendix C. Decomposing the mean and eddy energetics

In this section, we derive the mean and eddy KE equations. Equation (7) can be split into its mean and eddy component:

$$\frac{D^\#}{Dt}\boldsymbol{\nabla}_{\mathrm{h}}^2 \overline{\psi} + \frac{D^\#}{Dt}\boldsymbol{\nabla}_{\mathrm{h}}^2 \psi' + \boldsymbol{u}_g' \cdot \boldsymbol{\nabla}_{\mathrm{h}}[\boldsymbol{\nabla}_{\mathrm{h}}^2(\overline{\psi} + \psi')] + \beta \partial_x(\overline{\psi} + \psi') = f_0 \partial_z(\overline{w} + w'), \tag{A12}$$

where $\frac{D^\#}{Dt} = \partial_t + \overline{\boldsymbol{u}_g} \cdot \boldsymbol{\nabla}_{\mathrm{h}}$. Multiplying this by $-\overline{\psi}$ gives:

$$\begin{aligned}\frac{D^\#}{Dt}\frac{|\boldsymbol{\nabla}_{\mathrm{h}}\overline{\psi}|^2}{2} - \boldsymbol{\nabla}_{\mathrm{h}} \cdot \overline{\boldsymbol{u}_g}\overline{\psi}\boldsymbol{\nabla}_{\mathrm{h}}^2\overline{\psi} - \overline{\psi}\frac{D^\#}{Dt}\boldsymbol{\nabla}_{\mathrm{h}}^2\psi' - \overline{\psi}\boldsymbol{u}_g' \cdot \boldsymbol{\nabla}_{\mathrm{h}}[\boldsymbol{\nabla}_{\mathrm{h}}^2(\overline{\psi} + \psi')] \\ - \beta \partial_x \frac{\overline{\psi}^2}{2} - \overline{\psi}\beta\partial_x\psi' = \overline{w}\overline{b} - \overline{\psi} f_0 \partial_z w',\end{aligned} \tag{A13}$$

and taking its ensemble mean yields the mean KE equation:

$$\frac{D^\#}{Dt}\frac{|\boldsymbol{\nabla}_{\mathrm{h}}\overline{\psi}|^2}{2} - \boldsymbol{\nabla}_{\mathrm{h}} \cdot \overline{\boldsymbol{u}_g}\overline{\psi}\boldsymbol{\nabla}_{\mathrm{h}}^2\overline{\psi} - \beta\partial_x\frac{\overline{\psi}^2}{2} = \overline{w}\overline{b} + \overline{\psi}\boldsymbol{\nabla}_{\mathrm{h}} \cdot \overline{\boldsymbol{u}_g'\boldsymbol{\nabla}_{\mathrm{h}}^2\psi'}. \tag{A14}$$

On the other hand, the ensemble mean of total KE equation (17) is:

$$\overline{\frac{D}{Dt}\frac{|\boldsymbol{\nabla}_{\mathrm{h}}\psi|^2}{2}} - \boldsymbol{\nabla}_{\mathrm{h}} \cdot \overline{\boldsymbol{u}_g\psi\boldsymbol{\nabla}_{\mathrm{h}}^2\psi} - \beta\partial_x\frac{\overline{\psi^2}}{2} = \overline{wb}, \tag{A15}$$

 doi:10.20944/preprints202104.0283.v1

which can be expanded as:

$$\frac{D^\#}{Dt}\frac{|\nabla_\mathrm{h}\overline{\psi}|^2}{2} + \frac{D^\#}{Dt}\frac{\overline{|\nabla_\mathrm{h}\psi'|^2}}{2} + \nabla_\mathrm{h}\cdot\overline{\boldsymbol{u}'_g\frac{|\nabla_\mathrm{h}\psi'|^2}{2}} + \overline{\boldsymbol{u}'_g\cdot\nabla_\mathrm{h}(\partial_x\overline{\psi}\partial_x\psi' + \partial_y\overline{\psi}\partial_y\psi')}$$
$$- \nabla_\mathrm{h}\cdot\overline{\boldsymbol{u}_g\psi\nabla_\mathrm{h}^2\psi} - \beta\partial_x\frac{\overline{\psi^2}}{2} = \overline{wb}. \tag{A16}$$

Taking the difference between equations (A14) and (A16) gives the eddy KE equation:

$$\frac{D^\#}{Dt}\frac{\overline{|\nabla_\mathrm{h}\psi'|^2}}{2} + \nabla_\mathrm{h}\cdot\overline{\boldsymbol{u}'_g\frac{|\nabla_\mathrm{h}\psi'|^2}{2}} + \nabla_\mathrm{h}\cdot\overline{\boldsymbol{u}'_g(\partial_x\overline{\psi}\partial_x\psi' + \partial_y\overline{\psi}\partial_y\psi')}$$
$$- \nabla_\mathrm{h}\cdot\left(\overline{\boldsymbol{u}_g\psi\nabla_\mathrm{h}^2\psi} - \overline{\boldsymbol{u}_g}\overline{\psi}\nabla_\mathrm{h}^2\overline{\psi}\right) - \beta\partial_x\frac{\overline{\psi'^2}}{2} = \overline{w'b'} - \overline{\psi}\nabla_\mathrm{h}\cdot\overline{\boldsymbol{u}'_g\nabla_\mathrm{h}^2\psi'}. \tag{A17}$$

Since the divergence terms vanish upon area integration, we can see the mean and eddy KE exchanging the term $-\overline{\psi}\nabla_\mathrm{h}\cdot\overline{\boldsymbol{u}'_g\nabla_\mathrm{h}^2\psi'}$ (equations (A14) and (A17)). The same procedure can be done for equation (9) or the buoyancy equation to derive the mean and eddy APE equations.

Appendix D. The three-layer QG Lorenz energy cycle

The Lorenz energy cycle [2] for the first layer dropping the divergence terms in equations (A14) and (A17) while bringing back the viscous and diffusive terms becomes:

$$\partial_t K_1^\# = f_0\left[\overline{w_{a;1}}\overline{\psi_1^\dagger} + H_1\overline{w_{a;1}}\frac{\overline{\psi_1}-\overline{\psi_2}}{H_2+H_1}\right] + H_1\overline{\psi_1}\nabla_\mathrm{h}\cdot\overline{\boldsymbol{u}'_{g;1}\nabla_\mathrm{h}^2\psi'_1}$$
$$- \overline{\psi_1}\nabla_\mathrm{h}\times\boldsymbol{\tau} + H_1\overline{\psi_1}\nu_4\nabla_\mathrm{h}^4(\nabla_\mathrm{h}^2\overline{\psi_1}), \tag{A18}$$

$$\partial_t\mathcal{K}_1 = f_0\left[\overline{w'_{a;1}\psi_1^{\dagger\prime}} + H_1\overline{w'_{a;1}\frac{\psi'_1-\psi'_2}{H_2+H_1}}\right] - H_1\overline{\psi_1}\nabla_\mathrm{h}\cdot\overline{\boldsymbol{u}'_{g;1}\nabla_\mathrm{h}^2\psi'_1} + H_1\overline{\psi'_1\nu_4\nabla_\mathrm{h}^4(\nabla_\mathrm{h}^2\psi'_1)}, \tag{A19}$$

$$\partial_t P_1^\# = -f_0\overline{w_{a;1}}(\overline{\psi_1}-\overline{\psi_2}) - \frac{f_0^2}{g'_1}(\overline{\psi_1}-\overline{\psi_2})\nabla_\mathrm{h}\cdot\overline{\boldsymbol{u}^{\dagger\prime}_{g;1}(\psi'_1-\psi'_2)}$$
$$- \frac{f_0^2}{g'_1}(\overline{\psi_1}-\overline{\psi_2})\kappa_4\nabla_\mathrm{h}^4(\overline{\psi_1}-\overline{\psi_2}) - \frac{f_0^2(\overline{\psi_1}-\overline{\psi_2})^2}{2}\partial_t g_1'^{-1}, \tag{A20}$$

$$\partial_t\mathcal{P}_1 = -f_0\overline{w'_{a;1}(\psi'_1-\psi'_2)} + \frac{f_0^2}{g'_1}(\overline{\psi_1}-\overline{\psi_2})\nabla_\mathrm{h}\cdot\overline{\boldsymbol{u}^{\dagger\prime}_{g;1}(\psi'_1-\psi'_2)}$$
$$- \frac{f_0^2}{g'_1}\overline{(\psi'_1-\psi'_2)\kappa_4\nabla_\mathrm{h}^4(\psi'_1-\psi'_2)} - \frac{f_0^2\overline{(\psi'_1-\psi'_2)^2}}{2}\partial_t g_1'^{-1}. \tag{A21}$$

For the second layer:

$$\partial_t K_2^\# = f_0\left[-(\overline{w_{a;1}}\overline{\psi_1^\dagger} - \overline{w_{a;2}}\overline{\psi_2^\dagger}) + H_2\left(\overline{w_{a;1}}\frac{\overline{\psi_1}-\overline{\psi_2}}{H_2+H_1} + \overline{w_{a;2}}\frac{\overline{\psi_2}-\overline{\psi_3}}{H_3+H_2}\right)\right]$$
$$+ H_2\overline{\psi_2}\nabla_\mathrm{h}\cdot\overline{\boldsymbol{u}'_{g;2}\nabla_\mathrm{h}^2\psi'_2} + H_2\overline{\psi_2}\nu_4\nabla_\mathrm{h}^4(\nabla_\mathrm{h}^2\overline{\psi_2}), \tag{A22}$$

$$\partial_t\mathcal{K}_2 = f_0\left[-(\overline{w'_{a;1}\psi_1^{\dagger\prime}} - \overline{w'_{a;2}\psi_2^{\dagger\prime}}) + H_2\left(\overline{w'_{a;1}\frac{\psi'_1-\psi'_2}{H_2+H_1}} + \overline{w'_{a;2}\frac{\psi'_2-\psi'_3}{H_3+H_2}}\right)\right]$$
$$- H_2\overline{\psi_2}\nabla_\mathrm{h}\cdot\overline{\boldsymbol{u}'_{g;2}\nabla_\mathrm{h}^2\psi'_2} + H_2\overline{\psi'_2\nu_4\nabla_\mathrm{h}^4(\nabla_\mathrm{h}^2\psi'_2)}, \tag{A23}$$

Preprints (www.preprints.org) | NOT PEER-REVIEWED | Posted: 12 April 2021 doi:10.20944/preprints202104.0283.v1

$$\partial_t P_2^\# = -f_0\overline{w_{a;2}}(\overline{\psi_2}-\overline{\psi_3}) - \frac{f_0^2}{g_2'}(\overline{\psi_3}-\overline{\psi_2})\boldsymbol{\nabla}_\mathrm{h}\cdot\overline{\boldsymbol{u}^\dagger_{g;2}{}'(\psi_3'-\psi_2')} - \frac{f_0^2}{g_2'}(\overline{\psi_3}-\overline{\psi_2})\kappa_4\boldsymbol{\nabla}_\mathrm{h}^4(\overline{\psi_3}-\overline{\psi_2}), \tag{A24}$$

$$\partial_t \mathcal{P}_2 = -f_0\overline{w'_{a;2}(\psi_2'-\psi_3')} + \frac{f_0^2}{g_2'}(\overline{\psi_3}-\overline{\psi_2})\boldsymbol{\nabla}_\mathrm{h}\cdot\overline{\boldsymbol{u}^\dagger_{g;2}{}'(\psi_3'-\psi_2')} - \frac{f_0^2}{g_2'}\overline{(\psi_3'-\psi_2')\kappa_4\boldsymbol{\nabla}_\mathrm{h}^4(\psi_3'-\psi_2')}. \tag{A25}$$

For the third layer:

$$\begin{aligned}\partial_t K_3^\# = f_0\Big[-\overline{w_{a;2}}\,\overline{\psi_2^\dagger} + H_3\overline{w_{a;2}}\frac{\overline{\psi_2}-\overline{\psi_3}}{H_3+H_2}\Big] &+ H_3\overline{\psi_3}\boldsymbol{\nabla}_\mathrm{h}\cdot\overline{\boldsymbol{u}'_{g;3}\boldsymbol{\nabla}_\mathrm{h}^2\psi_3'} \\ &+ H_3\overline{\psi_3}[\nu_4\boldsymbol{\nabla}_\mathrm{h}^4(\boldsymbol{\nabla}_\mathrm{h}^2\overline{\psi_3})+\epsilon\boldsymbol{\nabla}_\mathrm{h}^2\overline{\psi_3}],\end{aligned} \tag{A26}$$

$$\begin{aligned}\partial_t \mathcal{K}_3 = f_0\Big[-\overline{w'_{a;2}\psi_2^{\dagger\prime}} + H_3\overline{w'_{a;2}\frac{\psi_2'-\psi_3'}{H_3+H_2}}\Big] &- H_3\overline{\psi_3}\nabla_\mathrm{h}\cdot\overline{\boldsymbol{u}'_{g;3}\boldsymbol{\nabla}_\mathrm{h}^2\psi_3'} \\ &+ H_3\overline{\psi_3'[\nu_4\boldsymbol{\nabla}_\mathrm{h}^4(\boldsymbol{\nabla}_\mathrm{h}^2\psi_3')+\epsilon\boldsymbol{\nabla}_\mathrm{h}^2\psi_3']}.\end{aligned} \tag{A27}$$

Although the biharmonic diffusive terms in the APE equations (A20), (A21), (A24) and (A25), which originate from diffusive terms in the layer-thickness equation (8), are applied solely for numerical stability and their similarity with buoyancy in primitive equations, their formulation is conceptually similar to the Gent-McWilliams' skew diffusivity [GM; 45]. GM represents the process of baroclinic instability upon which isopycnal displacements are smoothed out adiabatically within the isopycnal layer. Considering the quasi two-dimensional and adiabatic nature of the QG system, the interpretation of layer-thickness diffusivity becomes similar to the GM skew diffusivity. A major difference here is that the diffusivity is set as the bihamonic diffusivity and as such, should be negligible in damping the resolved eddies [11,31].

References

1. Phillips, N.A. The general circulation of the atmosphere: A numerical experiment. *Quarterly Journal of the Royal Meteorological Society* **1956**, *82*, 123–164. doi:10.1002/qj.49708235202.
2. Lorenz, E.N. *The nature and theory of the general circulation of the atmosphere*; Vol. 218, World Meteorological Organization, Geneva, Switzerland, 1967.
3. Holland, W.R. The role of mesoscale eddies in the general circulation of the ocean—Numerical experiments using a wind-driven quasi-geostrophic model. *Journal of Physical Oceanography* **1978**, *8*, 363–392. doi:10.1175/1520-0485(1978)008<0363:TROMEI>2.0.CO;2.
4. Kang, D.; Curchitser, E.N. Energetics of Eddy–Mean Flow Interactions in the Gulf Stream Region. *Journal of Physical Oceanography* **2015**, *45*, 1103–1120. doi:10.1175/JPO-D-14-0200.1.
5. McWilliams, J.C. A perspective on the legacy of Edward Lorenz. *Earth and Space Science* **2019**, *6*, 336–350. doi:10.1029/2018EA000434.
6. Vallis, G.K. *Atmospheric and oceanic fluid dynamics*, 2 ed.; Cambridge University Press, Cambridge, United Kingdom, 2017.
7. Su, Z.; Wang, J.; Klein, P.; Thompson, A.F.; Menemenlis, D. Ocean submesoscales as a key component of the global heat budget. *Nature Communications* **2018**, *9*. doi:10.1038/s41467-018-02983-w.
8. Ajayi, A.; Le Sommer, J.; Chassignet, E.; Molines, J.M.; Xu, X.; Albert, A.; Cosme, E. Spatial and Temporal Variability of the North Atlantic Eddy Field From Two Kilometric-Resolution Ocean Models. *Journal of Geophysical Research: Oceans* **2020**, *125*, e2019JC015827. doi:10.1029/2019JC015827.
9. Lévy, M.; Franks, P.J.; Smith, K.S. The role of submesoscale currents in structuring marine ecosystems. *Nature communications* **2018**, *9*, 1–16. doi:10.1038/s41467-018-07059-3.
10. McWilliams, J.C. Submesoscale currents in the ocean. *Proceedings of the Royal Society A: Mathematical, Physical and Engineering Sciences* **2016**, *472*, 20160117. doi:10.1098/rspa.2016.0117.
11. Uchida, T.; Balwada, D.; Abernathey, R.; McKinley, G.; Smith, S.; Levy, M. The contribution of submesoscale over mesoscale eddy iron transport in the open Southern Ocean. *Journal of Advances in Modeling Earth Systems* **2019**, *11*, 3934–3958. doi:10.1029/2019MS001805.
12. Charney, J.G. Geostrophic turbulence. *Journal of the Atmospheric Sciences* **1971**, *28*, 1087–1095. doi:10.1175/1520-0469(1971)028<1087:GT>2.0.CO;2.
13. Arbic, B.K.; Polzin, K.L.; Scott, R.B.; Richman, J.G.; Shriver, J.F. On eddy viscosity, energy cascades, and the horizontal resolution of gridded satellite altimeter products. *Journal of Physical Oceanography* **2013**, *43*, 283–300. doi:10.1175/JPO-D-11-0240.1.
14. Aluie, H.; Hecht, M.; Vallis, G.K. Mapping the Energy Cascade in the North Atlantic Ocean: The Coarse-Graining Approach. *Journal of Physical Oceanography* **2018**, *48*, 225–244. doi:10.1175/jpo-d-17-0100.1.

15. Thomas, L.N.; Tandon, A.; Mahadevan, A. Submesoscale processes and dynamics. *Ocean modeling in an Eddying Regime* **2008**, *177*, 17–38. doi:10.1029/177GM04.
16. Yang, Y.; McWilliams, J.C.; Liang, X.S.; Zhang, H.; Weisberg, R.H.; Liu, Y.; Menemenlis, D. Spatial and Temporal Characteristics of the Submesoscale Energetics in the Gulf of Mexico. *Journal of Physical Oceanography* **2020**. doi:10.1175/jpo-d-20-0247.1.
17. Qiu, B.; Chen, S.; Klein, P.; Sasaki, H.; Sasai, Y. Seasonal mesoscale and submesoscale eddy variability along the North Pacific Subtropical Countercurrent. *Journal of Physical Oceanography* **2014**, *44*, 3079–3098. doi:10.1175/JPO-D-14-0071.1.
18. Sasaki, H.; Klein, P.; Qiu, B.; Sasai, Y. Impact of oceanic-scale interactions on the seasonal modulation of ocean dynamics by the atmosphere. *Nature communications* **2014**, *5*, 1–8. doi:10.1038/ncomms6636.
19. Uchida, T.; Abernathey, R.; Smith, S. Seasonality of eddy kinetic energy in an eddy permitting global climate model. *Ocean Modelling* **2017**, *118*, 41–58. doi:10.1016/j.ocemod.2017.08.006.
20. Dong, J.; Fox-Kemper, B.; Zhang, H.; Dong, C. The seasonality of submesoscale energy production, content, and cascade. *Geophysical Research Letters* **2020**. doi:10.1029/2020gl087388.
21. Schubert, R.; Jonathan, G.; Greatbatch, R.J.; Baschek, B.; Biastoch, A. The Submesoscale Kinetic Energy Cascade: Mesoscale Absorption of Submesoscale Mixed-Layer Eddies and Frontal Downscale Fluxes. *Journal of Physical Oceanography* **2020**. doi:10.1175/JPO-D-19-0311.1.
22. Ajayi, A.; Le Sommer, J.; Chassignet, E.; Molines, J.M.; Xu, X.; Albert, A.; Dewar, W.K. Diagnosing cross-scale kinetic energy exchanges from two submesoscale permitting ocean models. *Journal of Advances in Modeling Earth Systems* **2021**.
23. Fox-Kemper, B.; Ferrari, R.; Hallberg, R. Parameterization of mixed layer eddies. Part I: Theory and diagnosis. *Journal of Physical Oceanography* **2008**, *38*, 1145–1165. doi:10.1175/2007JPO3792.1.
24. Johnson, L.; Lee, C.M.; D'Asaro, E.A. Global Estimates of Lateral Springtime Restratification. *Journal of Physical Oceanography* **2016**, *46*, 1555–1573. doi:10.1175/jpo-d-15-0163.1.
25. Thompson, A.F.; Lazar, A.; Buckingham, C.; Naveira Garabato, A.C.; Damerell, G.M.; Heywood, K.J. Open-Ocean Submesoscale Motions: A Full Seasonal Cycle of Mixed Layer Instabilities from Gliders. *Journal of Physical Oceanography* **2016**, *46*, 1285–1307. doi:10.1175/jpo-d-15-0170.1.
26. Bachman, S.; Fox-Kemper, B.; Bryan, F. A tracer-based inversion method for diagnosing eddy-induced diffusivity and advection. *Ocean Modelling* **2015**, *86*, 1–14.
27. Young, W.R. An Exact Thickness-Weighted Average Formulation of the Boussinesq Equations. *Journal of Physical Oceanography* **2012**, *42*, 692–707. doi:10.1175/jpo-d-11-0102.1.
28. Deremble, B.; Martinez, E.M. `MSOM`: Multiple Scale Ocean Model, 2020. doi:10.5281/zenodo.4669909.
29. Verron, J. Nudging satellite altimeter data into quasi-geostrophic ocean models. *Journal of Geophysical Research: Oceans* **1992**, *97*, 7479–7491. doi:10.1029/92JC00200.
30. Barnier, B.; Le Provost, C. Influence of bottom topography roughness on the jet and inertial recirculation of a mid-latitude gyre. *Dynamics of atmospheres and oceans* **1993**, *18*, 29–65. doi:10.1016/0377-0265(93)90003-P.
31. Hallberg, R. Using a resolution function to regulate parameterizations of oceanic mesoscale eddy effects. *Ocean Modelling* **2013**, *72*, 92–103. doi:10.1016/j.ocemod.2013.08.007.
32. Chelton, D.B.; DeSzoeke, R.A.; Schlax, M.G.; El Naggar, K.; Siwertz, N. Geographical variability of the first baroclinic Rossby radius of deformation. *Journal of Physical Oceanography* **1998**, *28*, 433–460. doi:10.1175/1520-0485(1998)028<0433:GVOTFB>2.0.CO;2.
33. Dijkstra, H.A.; Wubs, F.W.; Cliffe, A.K.; Doedel, E.; Dragomirescu, I.F.; Eckhardt, B.; Gelfgat, A.Y.; Hazel, A.L.; Lucarini, V.; Salinger, A.G.; others. Numerical bifurcation methods and their application to fluid dynamics: analysis beyond simulation. *Communications in Computational Physics* **2014**, *15*, 1–45. doi:10.4208/cicp.240912.180613a.
34. Pedlosky, J. *Geophysical fluid dynamics*, 2 ed.; Springer-Verlag, New York, USA, 1987.
35. Hoskins, B.J.; Draghici, I.; Davies, H.C. A new look at the ω-equation. *Quarterly Journal of the Royal Meteorological Society* **1978**, *104*, 31–38. doi:10.1002/qj.49710443903.
36. Gill, A.E. *Atmosphere-ocean dynamics*; Vol. 30, Academic Press, 1982; p. 662p.
37. Grooms, I.; Julien, K.; Fox-Kemper, B. On the interactions between planetary geostrophy and mesoscale eddies. *Dynamics of atmospheres and oceans* **2011**, *51*, 109–136. doi:10.1016/j.dynatmoce.2011.02.002.
38. Jamet, Q.; Deremble, B.; Wienders, N.; Uchida, T.; Dewar, W.K. On Wind-driven Energetics of Subtropical Gyres. *Journal of Advances in Modelling Earth Systems* **2021**, p. e2020MS002329. doi:10.1029/2020MS002329.
39. Sérazin, G.; Jaymond, A.; Leroux, S.; Penduff, T.; Bessières, L.; Llovel, W.; Barnier, B.; Molines, J.M.; Terray, L. A global probabilistic study of the ocean heat content low-frequency variability: Atmospheric forcing versus oceanic chaos. *Geophysical Research Letters* **2017**, *44*, 5580–5589. doi:10.1002/2017GL073026.
40. Leroux, S.; Penduff, T.; Bessières, L.; Molines, J.M.; Brankart, J.M.; Sérazin, G.; Barnier, B.; Terray, L. Intrinsic and Atmospherically Forced Variability of the AMOC: Insights from a Large-Ensemble Ocean Hindcast. *Journal of Climate* **2018**, *31*, 1183–1203. doi:10.1175/jcli-d-17-0168.1.
41. Jamet, Q.; Dewar, W.K.; Wienders, N.; Deremble, B. Spatiotemporal Patterns of Chaos in the Atlantic Overturning Circulation. *Geophysical Research Letters* **2019**, *46*, 7509–7517. doi:10.1029/2019GL082552.
42. Khatri, H.; Sukhatme, J.; Kumar, A.; Verma, M.K. Surface ocean enstrophy, kinetic energy fluxes, and spectra from satellite altimetry. *Journal of Geophysical Research: Oceans* **2018**, *123*, 3875–3892. doi:10.1029/2017JC013516.

 doi:10.20944/preprints202104.0283.v1

43. Penduff, T.; Juza, M.; Brodeau, L.; Smith, G.C.; Barnier, B.; Molines, J.M.; Treguier, A.M.; Madec, G. Impact of global ocean model resolution on sea-level variability with emphasis on interannual time scales. *Ocean Science* **2010**, *6*, 269–284. doi:10.5194/os-6-269-2010.
44. Hoyer, S.; Hamman, J.; Roos, M.; Cherian, D.; Fitzgerald, C.; others. `xarray`: N-D labeled arrays and datasets, 2020. doi:10.5281/zenodo.4299126.
45. Griffies, S.M. The Gent–McWilliams skew flux. *Journal of Physical Oceanography* **1998**, *28*, 831–841.